

A new measurement of the structure functions $P_{LL} - P_{TT}/\varepsilon$ and P_{LT} in virtual Compton scattering at $Q^2 = 0.33 \text{ (GeV}/c)^2$

The A1 Collaboration

P. Janssens¹, L. Doria², P. Achenbach², C. Ayerbe Gayoso², D. Baumann², J.C. Bernauer², I.K. Bensafa³, R. Böhm², D. Bosnar⁴, E. Burtin⁵, N. D'Hose⁵, X. Defay³, M. Ding², M.O. Distler², H. Fonvielle^{3,a}, J. Friedrich², J.M. Friedrich⁶, G. Laveissière³, M. Makek⁴, J. Marroncle⁵, H. Merkel², U. Müller², L. Nungesser², B. Pasquini⁷, J. Pochodzalla², O. Postavaru¹⁰, M. Potokar⁸, D. Ryckbosch¹, S. Sanchez Majos², B.S. Schlimme², M. Seimetz⁵, S. Širca^{8,9}, G. Tamas², R. Van de Vyver¹, L. Van Hoorebeke¹, A. Van Overloop¹, Th. Walcher², and M. Weinrieger²

¹ Department of Subatomic and Radiation Physics, University of Gent, 9000 Gent, Belgium

² Institut für Kernphysik, Johannes Gutenberg-Universität, 55099 Mainz, Germany

³ LPC, Université Blaise Pascal, IN2P3, 63177 Aubière Cedex, France

⁴ Department of Physics, University of Zagreb, 10002 Zagreb, Croatia

⁵ CEA DAPNIA-SPhN, C.E. Saclay, 91191 Gif-sur-Yvette Cedex, France

⁶ Physik-Department, Technische Universität München, 85748 Garching, Germany

⁷ Dipartimento di Fisica Nucleare e Teorica, Università degli Studi di Pavia, and INFN, Sezione di Pavia, Pavia, Italy

⁸ Jožef Stefan Institute, Ljubljana, Slovenia

⁹ Department of Physics, University of Ljubljana, Slovenia

¹⁰ Institute of Space Science, RO-76900, Bucharest-Magurele, Romania

Received: 7 March 2008 / Revised: 16 May 2008

Published online: 16 July 2008 – © Società Italiana di Fisica / Springer-Verlag 2008

Communicated by Z.-E. Meziani

Abstract. The cross-section of the $ep \rightarrow e'p'\gamma$ reaction has been measured at $Q^2 = 0.33 \text{ (GeV}/c)^2$. The experiment was performed using the electron beam of the MAMI accelerator and the standard detector setup of the A1 Collaboration. The cross-section is analyzed using the low-energy theorem for virtual Compton scattering, yielding a new determination of the two structure functions $P_{LL} - P_{TT}/\varepsilon$ and P_{LT} which are linear combinations of the generalized polarizabilities of the proton. We find somewhat larger values than in the previous investigation at the same Q^2 . This difference, however, is purely due to our more refined analysis of the data. The results tend to confirm the non-trivial Q^2 -evolution of the generalized polarizabilities and call for more measurements in the low- Q^2 region ($\leq 1 \text{ (GeV}/c)^2$).

PACS. 13.60.Fz Elastic and Compton scattering – 14.20.Dh Protons and neutrons – 25.30.Rw Electroproduction reactions

1 Introduction

The internal structure of the proton can be studied using virtual Compton scattering (VCS). In this reaction ($\gamma^*p \rightarrow \gamma p'$) a virtual photon γ^* scatters off the proton p and a real photon γ is produced. The VCS reaction below the pion production threshold allows to measure the generalized polarizabilities of the proton (GPs) [1–4]. These GPs are functions of the photon four-momentum transfer squared Q^2 and they describe the polarizability locally inside the proton on a distance scale indicated by Q^2 [5]. Among the six lowest-order dipole GPs, two are an extension of the polarizabilities α_E and β_M obtained in real

Compton scattering (RCS) [6], quantifying the deformation of the charge and magnetization distributions inside the proton caused by a static electric or magnetic field, respectively.

VCS is accessed through photon electroproduction ($ep \rightarrow e'p'\gamma$) as shown in fig. 1. \mathbf{k} , \mathbf{p} and \mathbf{q} are the three-momentum vectors of the incoming electron and proton, and the virtual photon, respectively¹. \mathbf{k}' , \mathbf{p}' and \mathbf{q}' are the three-momentum vectors of the outgoing particles. Five independent variables are necessary to define the

¹ All variables defined in the center of mass of the virtual photon and target proton have an index “cm”. If no index is given the variable is defined in the laboratory system.

^a e-mail: helene@cclermont.in2p3.fr

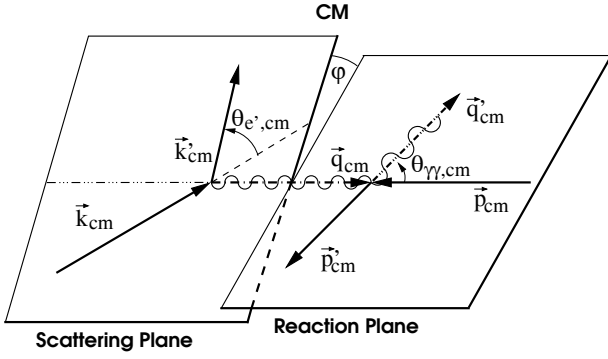


Fig. 1. Schematic drawing of the $ep \rightarrow e'p'\gamma$ reaction in the center of mass of the virtual photon and the target proton.

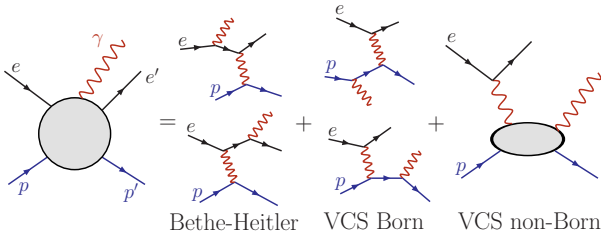


Fig. 2. Contributions to the $ep \rightarrow e'p'\gamma$ reaction.

kinematics of the reaction, *e.g.* the modulus of the virtual photon momentum q_{cm} and its polarization parameter ε , the modulus of the real (outgoing) photon momentum q'_{cm} and the polar and azimuthal angles of the real photon with respect to the virtual photon direction, $\theta_{\gamma\gamma_{\text{cm}}}$ and φ , respectively. The five-fold differential cross-section $d^5\sigma/dk'd\Omega_{k'}d\Omega_{q'_{\text{cm}}}$ (with $k' = \text{modulus of } \mathbf{k}'$) will be noted $d^5\sigma$.

The photon electroproduction reaction contains three contributions (see fig. 2). The reaction is dominated by the Bethe-Heitler and Born (BH+B) contributions, where the outgoing photon is produced due to bremsstrahlung of the electron or proton, respectively. The contribution of the BH+B process can be calculated exactly based on the proton form factors. The GPs make up the VCS non-Born part of the reaction [2].

2 Experimental determination of the GPs

The GPs cannot be measured directly. In the physical observables (cross-sections and asymmetries) they appear in specific linear combinations, the structure functions. There are six independent GPs, and, by consequence, there are six independent structure functions [4]. Only three of them, denoted as P_{LL} , P_{TT} and P_{LT} , appear at leading order in the low-energy expansion of the unpolarized cross-section. The set of all six GPs can be obtained only by double-polarized VCS. Such an experiment was performed at MAMI recently for the first time [7] using a longitudinally polarized electron beam and measuring the recoil proton polarization. The analysis of the double polarization asymmetry [8,9] will be the subject of forthcoming publications. These data can also be used for the

determination of the unpolarized cross-section by neglecting the beam and recoil proton polarizations. The present paper reports the results of the unpolarized analysis from this experiment [8]. The same set of structure functions has been determined previously in several experiments at various values of Q^2 [10–12].

The low-energy theorem (LET) for virtual Compton scattering is used to expand the cross-section in powers of q'_{cm} ([2] and [4]):

$$d^5\sigma = d^5\sigma^{\text{BH+B}} + \phi q'_{\text{cm}} M_0^{\text{NB}} + \mathcal{O}(q'_{\text{cm}}{}^2), \quad (1)$$

where ϕ is a known phase-space factor, $d^5\sigma^{\text{BH+B}}$ is the five-fold differential cross-section for the BH+B process and M_0^{NB} , which contains the information about the GPs, is defined by

$$\frac{M_0^{\text{NB}}}{v_{\text{LT}}} = \frac{v_{\text{LL}}}{v_{\text{LT}}} (P_{\text{LL}} - P_{\text{TT}}/\varepsilon) + P_{\text{LT}}. \quad (2)$$

In this equation v_{LT} and v_{LL} are known kinematical functions of q_{cm} , ε , $\theta_{\gamma\gamma_{\text{cm}}}$ and φ (see, *e.g.*, ref. [4] for their complete definition). At fixed ε , two linear combinations of structure functions, $P_{\text{LL}} - P_{\text{TT}}/\varepsilon$ and P_{LT} , can be determined experimentally. The LET method assumes that, since the higher-order terms $\mathcal{O}(q'_{\text{cm}}{}^2)$ in eq. (1) are small for low q'_{cm} (a condition which holds below the pion production threshold), they can be neglected. The cross-section is measured in an appropriate kinematical region, *i.e.* covering a range large enough in v_{LL} and v_{LT} , here provided by a large coverage in $\theta_{\gamma\gamma_{\text{cm}}}$. Then one forms the quantity $M_0^{\text{NB}} = (d^5\sigma - d^5\sigma^{\text{BH+B}}) / (\phi q'_{\text{cm}})$, which is fitted to a linear combination of the two structure functions, as expressed by eq. (2).

3 Experimental setup and event analysis

For the present experiment the standard setup of the A1 Collaboration at MAMI was used [13] together with the polarized electron beam and the focal-plane proton polarimeter. These two items are not detailed here since they play no role in the unpolarized analysis. The beam from the MAMI accelerator impinged with an energy of 854.6 MeV on a liquid-hydrogen target. The temperature and pressure inside the target cell were constantly monitored and the beam charge was measured continuously by a Förster probe, allowing to determine the experimental luminosity \mathcal{L}_{exp} with good precision (well below 1%). The mean beam current was about 22 μA . To prevent local boiling of the hydrogen, the beam was deflected with an amplitude of a few mm and a frequency of a few kHz. The scattered electron and the recoiling proton were detected in the high-resolution spectrometers B and A, respectively. The setting of the spectrometers is given in table 1. This setting resulted in the central values $q_{\text{cm}} = 600 \text{ MeV}/c$, $q'_{\text{cm}} = 90 \text{ MeV}/c$, $\varepsilon = 0.645$ and $\varphi = 180^\circ$, and the spectrometer acceptance covered the range $[70, 180]^\circ$ for $\theta_{\gamma\gamma_{\text{cm}}}$.

Each spectrometer contains two sets of double-planes of vertical drift chambers for track reconstruction and two

Table 1. Parameters of the spectrometer setup for the VCS90b-setting: central momentum, in-plane angle (θ) and out-of-plane angle (ϕ_{oop}).

Parameter	Spectrometer A	Spectrometer B	Unit
p_{central}	645.4	539.4	MeV/c
θ	38.0	50.6	degrees
ϕ_{oop}	0.0	0.0	degrees

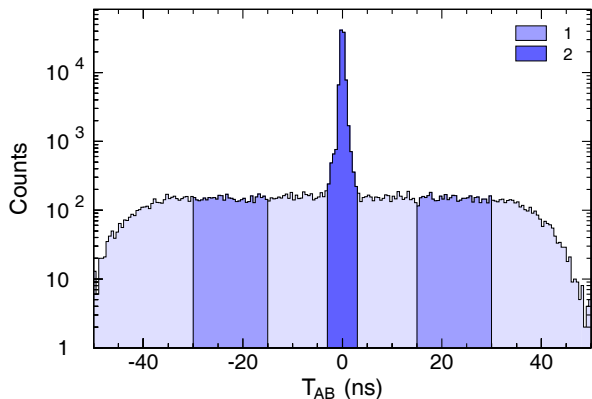


Fig. 3. Histogram of the coincidence time T_{AB} for events within the analysis cuts. The coincident events inside the central peak (distribution 2) are selected and distribution 1 is used for the subtraction of random coincidences.

scintillator planes for timing and particle identification. The gas Cherenkov counter in spectrometer B identifies electrons. At the proton side such a Cherenkov detector was not present, since the focal-plane polarimeter was mounted in spectrometer A.

The distribution of the coincidence time T_{AB} is shown in fig. 3. The coincident events are selected in a time window of 6 ns and a subtraction of the random coincidences is performed using the events inside $T_{AB} \in [-30, -15]$ ns and $T_{AB} \in [15, 30]$ ns. This correction is small since the random coincidences contribute to less than 2% to the central peak in fig. 3 (note the logarithmic scale).

Photon electroproduction events are identified by missing-mass reconstruction. The distribution of the square of the missing mass M_X^2 in $ep \rightarrow epX$, displayed in fig. 4, shows two peaks corresponding to γ and π^0 electroproduction. The π^0 peak is present because the acceptance, while centered on $q'_{\text{cm}} = 90$ MeV/c, extends above pion threshold. The separation between the two electroproduction processes is excellent (about 30 times the peak FWHM). For the calculation of the cross-section only the events with $M_X^2 \in [-1000, 2000]$ MeV²/c⁴ are used.

A cut on the target length has been applied to remove the events from the interactions of the incoming electrons with the end caps of the target, which are much more dense than the liquid hydrogen itself. Other cuts are necessary to select the events inside the desired kinematic range: $|q_{\text{cm}} - 600 \text{ MeV}/c| < 12 \text{ MeV}/c$, $|q'_{\text{cm}} - 90 \text{ MeV}/c| < 15 \text{ MeV}/c$, $|\varepsilon - 0.645| < 0.012$ and a range of $\pm 12^\circ$ for the out-of-plane angle of the outgoing photon. After these

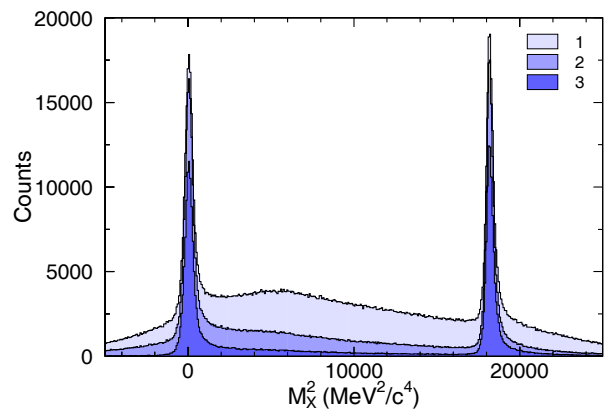


Fig. 4. Histogram of the square of the missing mass M_X^2 . Distribution 1 corresponds to the raw coincidences, while in distribution 2 only events within the central peak in T_{AB} are taken into account and the random coincidences are subtracted. In distribution 3 also the events in the region of the end caps of the target are removed.

cuts the signals of the scintillators and Cherenkov counters were used to estimate the remaining background processes, which were found to contribute to less than 0.5%. Since this is well below the statistical uncertainty of the experiment, no cut was applied on these detector signals. The count rates were corrected for the detector efficiency. However, this correction was very small and did not have any influence on the extracted structure functions.

4 Unpolarized cross-section and extraction of structure functions

For the determination of the cross-section the effective solid angle of the detection apparatus is calculated using a Monte Carlo simulation [14]. This Monte Carlo takes into account the detailed geometry of the apparatus, the beam configuration, and all resolution deteriorating effects, such as the intrinsic resolution of the detectors, energy losses in the materials of the target, etc. The events are generated according to the BH+B cross-section, which is used as an approximation of the real cross-section of the photon electroproduction reaction (the non-Born contribution will then be incorporated in an iterative procedure). Radiative effects are taken into account as explained in [15]: the acceptance-dependent part is included in the simulation and the remaining part, due to virtual corrections, is implemented by multiplying the experimental cross-section by a constant factor f_{cor} over the complete phase space. This factor equals 0.942 for the kinematics of the present experiment. The simulation reproduces the radiative tail very well, as can be seen in fig. 5. In this figure the simulated distribution is normalized using the factor $\mathcal{L}_{\text{exp}}/(\mathcal{L}_{\text{sim}}f_{\text{cor}})$, where \mathcal{L}_{sim} is the luminosity corresponding to the simulated events. The stability of the experimental cross-section *versus* different M_X^2 cuts is better than 1%.

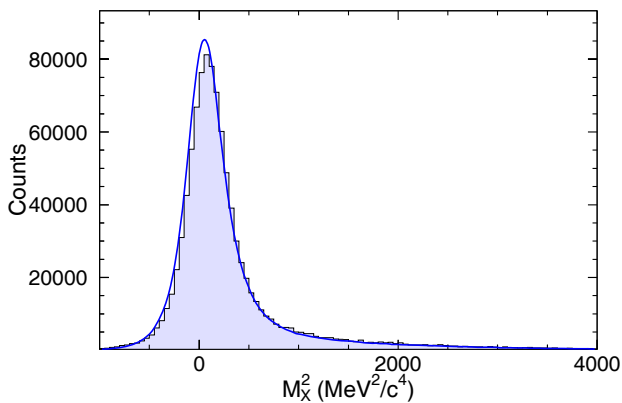


Fig. 5. Experimental (histogram) and simulated (full line) histogram of M_X^2 . Both distributions are obtained after applying all cuts. The slight offset in position between both maxima is discussed in the text.

The central momenta of the spectrometers were calibrated in absolute using the M_X^2 distribution. By simultaneously adjusting the experimental peak position (on the simulated one) and minimizing its width, one obtains the two central momenta. This adjustment was done on a kinematical phase space as wide as possible. For the subset of events within the analysis cuts, it results in a slight offset between the experimental and simulated peak positions (fig. 5), reflecting the uncertainty of the calibration. This uncertainty is estimated to be $\pm 3 \cdot 10^{-4}$ (in relative) of the central momentum of each spectrometer. It can fully account for the observed offset, *i.e.* peak positions in fig. 5 would coincide by changing either one momentum or the other within the quoted uncertainty.

We now explain the iteration method used to obtain the experimental ($ep \rightarrow e'p'\gamma$) cross-section. It is important to use the most realistic cross-section for the event generation in the simulation [14]. In a first step, using $d\sigma^{\text{BH+B}}$ in the simulation, one determines the experimental cross-section and extracts the structure functions $P_{\text{LL}} - P_{\text{TT}}/\varepsilon$ and P_{LT} , as explained in sect. 2. Then in a second step the cross-section in the simulation is modified to include the GP effect measured in the first step. The effective solid angle is recalculated, and the whole procedure is iterated several times. After three iterations a stable result is obtained. The effect of the iterations on the solid angle is shown in fig. 6a. The effect is small ($< 2\%$), but, due to its pronounced $\theta_{\gamma\gamma\text{cm}}$ -dependence, it has a substantial influence on the obtained structure functions (see sect. 5). Another feature is that the iteration procedure yields the same result, independent of the initial value for the structure functions. This is represented in fig. 6b. When the BH+B cross-section is used in the first step of the simulation, the starting point is $(P_{\text{LL}} - P_{\text{TT}}/\varepsilon, P_{\text{LT}}) = (0, 0) \text{ GeV}^{-2}$.

The final cross-section is displayed in fig. 7 and the cross-section values are given in table 2. The main sources of systematic uncertainties are the calibration of the momenta and angles of the reconstructed particles, the

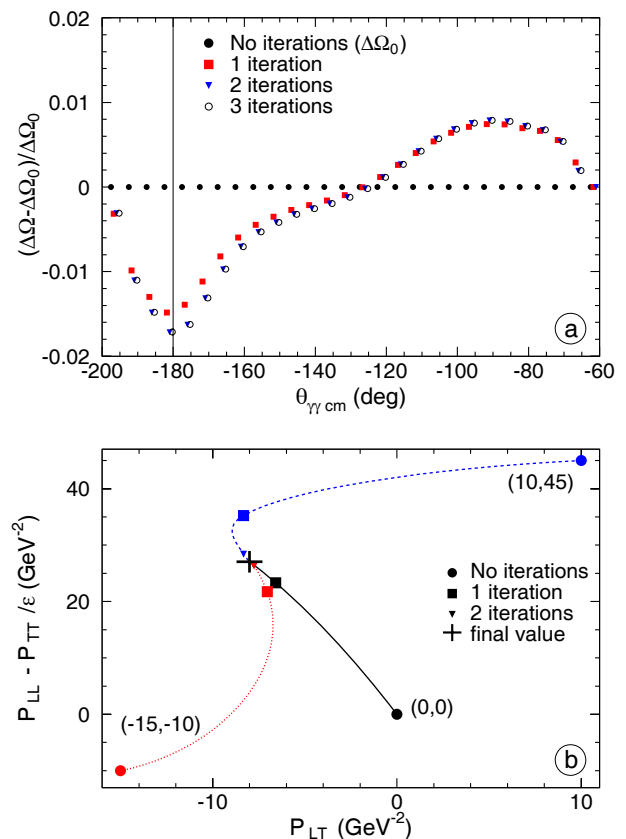


Fig. 6. a) Influence of the iteration procedure on the effective solid angle. The points at the left of $(\theta_{\gamma\gamma\text{cm}} = -180^\circ)$ correspond to $\varphi = 0^\circ$, the points at the right to $\varphi = 180^\circ$. b) Convergence pattern for three different starting points, represented by the values of $(P_{\text{LL}} - P_{\text{TT}}/\varepsilon, P_{\text{LT}})$ in parenthesis. The cross at the final point gives the size of the statistical uncertainty. The figure is obtained with the proton form factors of ref. [16] (see sect. 5).

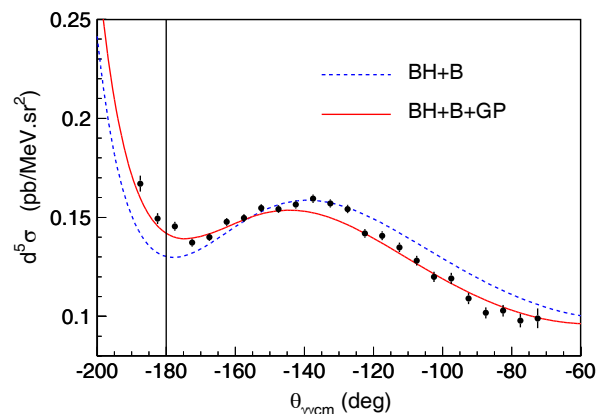


Fig. 7. The unpolarized $ep \rightarrow e'p'\gamma$ cross-section measured at $q_{\text{cm}}^L = 90 \text{ MeV}/c$, $q_{\text{cm}} = 600 \text{ MeV}/c$, $\varepsilon = 0.645$ and $\varphi = 180^\circ$. The dotted line shows the BH+B cross-section, calculated with the proton form factors of ref. [16]. The full line includes the effect of the structure functions obtained in the experiment (first line of table 5). The two most left points correspond to $\varphi = 0^\circ$.

Table 2. The $ep \rightarrow e'p'\gamma$ cross-section, in $\text{pb}/(\text{MeV}\cdot\text{sr}^2)$, obtained in this experiment (after iterations) at fixed $q'_{\text{cm}} = 90 \text{ MeV}/c$, $q_{\text{cm}} = 600 \text{ MeV}/c$ and $\varepsilon = 0.645$. The error is statistical only. The BH+B cross-section is calculated using the form factors of ref. [16].

$\theta_{\gamma\gamma\text{cm}}$	φ	$d^5\sigma^{\text{BH+B}}$	$d^5\sigma$
177.5°	180°	0.129	0.146 ± 0.002
172.5°	180°	0.132	0.137 ± 0.002
167.5°	180°	0.136	0.140 ± 0.002
162.5°	180°	0.142	0.148 ± 0.002
157.5°	180°	0.148	0.150 ± 0.002
152.5°	180°	0.153	0.155 ± 0.002
147.5°	180°	0.156	0.154 ± 0.002
142.5°	180°	0.158	0.156 ± 0.002
137.5°	180°	0.158	0.159 ± 0.002
132.5°	180°	0.157	0.157 ± 0.002
127.5°	180°	0.155	0.154 ± 0.002
122.5°	180°	0.151	0.142 ± 0.002
117.5°	180°	0.147	0.140 ± 0.002
112.5°	180°	0.142	0.135 ± 0.002
107.5°	180°	0.137	0.128 ± 0.002
102.5°	180°	0.132	0.120 ± 0.003
97.5°	180°	0.126	0.119 ± 0.003
92.5°	180°	0.122	0.109 ± 0.003
87.5°	180°	0.117	0.102 ± 0.003
82.5°	180°	0.113	0.103 ± 0.003
77.5°	180°	0.109	0.098 ± 0.003
72.5°	180°	0.106	0.099 ± 0.005
177.5°	0°	0.132	0.149 ± 0.003
172.5°	0°	0.141	0.167 ± 0.004

normalization of the cross-section (luminosity), the radiative corrections and the simulation of the solid angle. To study the first point, the central momenta of the spectrometers were changed by $\pm 3 \cdot 10^{-4}$ in relative and the data were re-analyzed, yielding new values for the cross-section (and the structure functions). The maximal deviation w.r.t. the original values was taken as the uncertainty due to momentum calibration. A procedure along the same lines allows to estimate the systematic error due to the uncertainty in the horizontal angle (spectrometer angle plus transfer matrix), taken equal to $\pm 0.1 \text{ mr}$ in each arm. These sources of error are $\theta_{\gamma\gamma\text{cm}}$ -dependent, changing the shape of the cross-section. The three other sources are $\theta_{\gamma\gamma\text{cm}}$ -independent; summed quadratically, they cause an error in the overall normalization of the cross-section of $\pm 2\%$. The statistical error on the cross-section is generally smaller, about $\pm 1.4\%$ for most data points (table 2).

The two structure functions $P_{LL} - P_{TT}/\varepsilon$ and P_{LT} are extracted by a linear fit of the quantity $M_0^{\text{NB}}/v_{\text{LT}}$ as a function of $v_{\text{LL}}/v_{\text{LT}}$. They are determined at a fixed value of $q_{\text{cm}} = 600 \text{ MeV}/c$, or equivalently at a fixed value of $Q^2 = 0.33 (\text{GeV}/c)^2$. The fit is performed via a χ^2 minimization, which also provides the statistical error on the

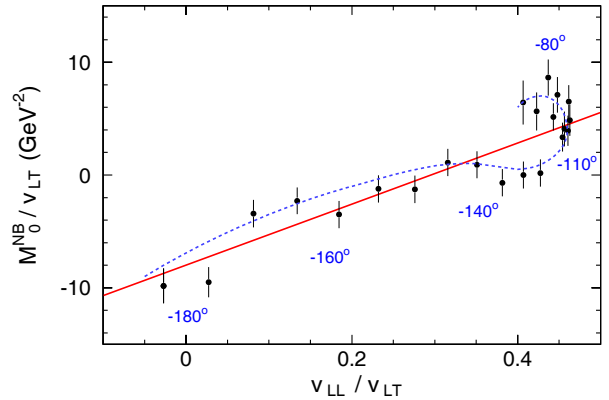


Fig. 8. The linear fit of the structure functions: $P_{LL} - P_{TT}/\varepsilon$ (slope) and P_{LT} (intercept). Error bars are statistical only. The angular values reported along the schematic dotted line show the evolution of the points with $\theta_{\gamma\gamma\text{cm}}$. The two extreme points $(\theta_{\gamma\gamma\text{cm}}, \varphi) = (72.5^\circ, 180^\circ)$ and $(172.5^\circ, 0^\circ)$ are removed from the fit. The figure is obtained with the proton form factors of ref. [16] and after final iteration.

Table 3. Estimation of the systematic error on the structure functions (in GeV^{-2}).

	$P_{LL} - P_{TT}/\varepsilon$	P_{LT}
Momentum calibration	± 2.7	± 1.0
Horizontal angles	± 1.2	± 0.4
Normalization of the cross-section	± 0.6	± 1.9
Total systematic error (quadr. sum)	± 3.0	± 2.2

structure functions. The result is shown in fig. 8. The reduced χ^2 of the fit, 2.6 for 20 d.o.f., suggests that the higher-order terms $\mathcal{O}(q'_{\text{cm}}{}^2)$ in eq. (1), although small, are not completely negligible. This effect of the LET truncation has not been considered in the error budget. The systematic errors on the structure functions are summarized in table 3, where, as for the cross-section, they are separated into an angle-dependent and an angle-independent part (first two lines and third line, respectively).

5 Discussion

The effect of the GPs in the photon electroproduction cross-section is small; in the kinematics of the experiment it reaches at maximum $\sim \pm 10\%$ (see fig. 7). Therefore any small change at the cross-section level may induce a relatively large change in the fitted structure functions.

A first example is provided by the iterative calculation of the solid angle, explained in sect. 4. Using this procedure, $P_{LL} - P_{TT}/\varepsilon$ is increased by 16% and P_{LT} by 20–30% (see tables 4 and 5). In the first VCS experiment at MAMI [11], this iterative procedure was not pushed to its convergence point, because its effect was smaller than the statistical uncertainty, at the cross-section level. Indeed, as can be seen in fig. 6a, the iterations change the

Table 4. Results for $P_{LL} - P_{TT}/\varepsilon$ and P_{LT} without the iterations for $q_{cm} = 600 \text{ MeV}/c$ using different form factor parameterizations. The first error is statistical, the second is the systematic one. ε in ref. [11] ($\varepsilon = 0.620$) was slightly different from the present experiment ($\varepsilon = 0.645$).

	$P_{LL} - P_{TT}/\varepsilon$ (GeV^{-2})	P_{LT} (GeV^{-2})	Form factor
This work	$23.3 \pm 1.9 \pm 3.0$	$-6.6 \pm 0.7 \pm 2.2$	[16]
	$24.3 \pm 1.9 \pm 3.0$	$-3.9 \pm 0.7 \pm 2.2$	[17, 18]
	$24.7 \pm 1.9 \pm 3.0$	$-8.9 \pm 0.7 \pm 2.2$	[19]
	$23.7 \pm 1.9 \pm 3.0$	$-5.3 \pm 0.7 \pm 2.2$	[20, 21]
Ref. [11]	$23.7 \pm 2.2 \pm 4.3$	$-5.0 \pm 0.8 \pm 1.8$	[20]

Table 5. Results for $P_{LL} - P_{TT}/\varepsilon$ and P_{LT} after applying the iteration procedure for $q_{cm} = 600 \text{ MeV}/c$ using different form factor parameterizations. The first error is statistical, the second is the systematic one.

	$P_{LL} - P_{TT}/\varepsilon$ (GeV^{-2})	P_{LT} (GeV^{-2})	Form factor
This work	$27.1 \pm 1.9 \pm 3.0$	$-8.0 \pm 0.7 \pm 2.2$	[16]
	$28.5 \pm 1.9 \pm 3.0$	$-5.2 \pm 0.7 \pm 2.2$	[17, 18]
	$28.6 \pm 1.9 \pm 3.0$	$-10.1 \pm 0.7 \pm 2.2$	[19]
	$27.4 \pm 1.9 \pm 3.0$	$-6.8 \pm 0.7 \pm 2.2$	[20, 21]

solid angle (and hence the cross-section) by less than 1% in the main part of the phase space, whereas the statistical uncertainty on the cross-section was $\sim 2\text{-}3\%$. Therefore the result of [11] is non-iterated. It can be compared to the non-iterated result of the present analysis, performed at the same value of q_{cm} . As shown in table 4, at this level the agreement is strikingly good between the two experiments.

A second example is provided by the form factor parameterizations (for recent reviews on nucleon form factors, see refs. [22] and [23]). The obtained structure functions depend on the choice made for the proton form factors G_E^p and G_M^p , because these observables enter the calculation of the BH+B cross-section. In this analysis various form factor parameterizations have been considered [16–21] (see fig. 9). Mainly P_{LT} is sensitive to this choice: going from the parameterization of ref. [20] (or [21]) to the other ones, P_{LT} changes by $(\begin{smallmatrix} +23 \\ -48 \end{smallmatrix})\%$ while $P_{LL} - P_{TT}/\varepsilon$ changes by 1–4% only (cf. table 5). This is caused by the fact that a change of form factor induces mainly a variation of the magnitude of the BH+B cross-section without affecting too much its $\theta_{\gamma\gamma_{cm}}$ -dependence (see fig. 9), resulting mostly in a change of the intercept in fig. 8.

It should be noted that in [11] the experimental cross-section was compared to the theoretical one also at very low q'_{cm} . This test favored the form factor parameterization of ref. [20] which was consequently chosen in the analysis, and an overall form factor uncertainty was embedded in the systematic error². The present experiment is only

² This uncertainty is accounted for in the last line of table 4.

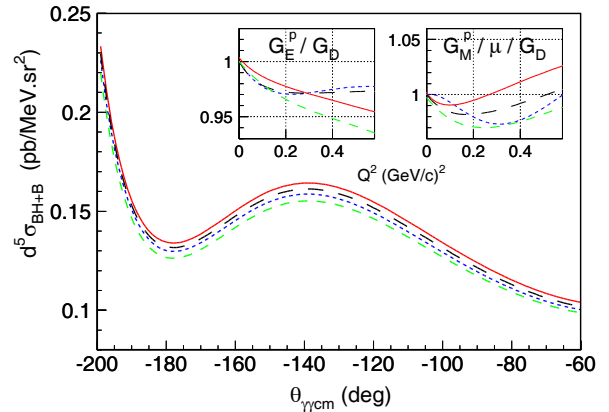


Fig. 9. The BH+B cross-section, at the kinematics of the experiment, for proton form factors as parameterized in [16] (dotted line), [17,18] (solid line), [19] (short-dashed line) and [20] (long-dashed line). The corresponding form factor parameterizations are shown in the insert, with $G_D = 1 + (Q^2/0.71 \text{ (GeV}/c)^2)^{-2}$. Reference [21] gives curves very similar to [20].

performed at $q'_{cm} = 90 \text{ MeV}/c$, preventing such normalization test at low q'_{cm} . The uncertainty due to the proton form factors is not included in the numerical value of the systematic error of table 5. It is represented explicitly by the four different lines of results in this table³.

The resulting structure functions are displayed in fig. 10 together with the other existing measurements. At low Q^2 they can be compared to a calculation in the framework of the heavy-baryon chiral perturbation theory (HBChPT) [24]. The calculation at order p^3 for the structure functions evaluated at $Q^2 = 0.33 \text{ (GeV}/c)^2$ and $\varepsilon = 0.645$ gives $P_{LL} - P_{TT}/\varepsilon = 25.5 \text{ GeV}^{-2}$ and $P_{LT} = -5.3 \text{ GeV}^{-2}$, in overall good agreement with the values measured in this experiment. At next order in HBChPT, only the spin GPs have been evaluated [25, 26]. A complete ChPT calculation of the present structure functions, combining scalar and spin GPs, is still to come. The dispersive formalism of refs. [27, 28] offers an alternative approach in which the electric and magnetic GPs can be fitted from the experiment. For a more extensive comparison to the theoretical models we refer the reader to, *e.g.*, ref. [29].

In the structure functions presented here, the contribution of the spin GPs (and hence P_{TT} , which contains only spin GPs) is expected to be small. Therefore the data for $P_{LL} - P_{TT}/\varepsilon$ essentially reflect the behavior of P_{LL} , which is proportional to the product $G_E^p \cdot \alpha_E$. The data do not follow a simple dipole shape over the full measured Q^2 range. To fix the shape, more measurements are needed in the region up to $1 \text{ (GeV}/c)^2$. For the structure function

³ If, however, one wants a single number for this systematic error, one may take the half-difference between the two extreme results of table 5, *i.e.* ± 0.7 (respectively, ± 2.4) GeV^{-2} for the first (respectively, second) structure function. This would give after quadratic sum a total systematic error of ± 3.1 (respectively, ± 3.3) GeV^{-2} on $P_{LL} - P_{TT}/\varepsilon$ (respectively, P_{LT}).

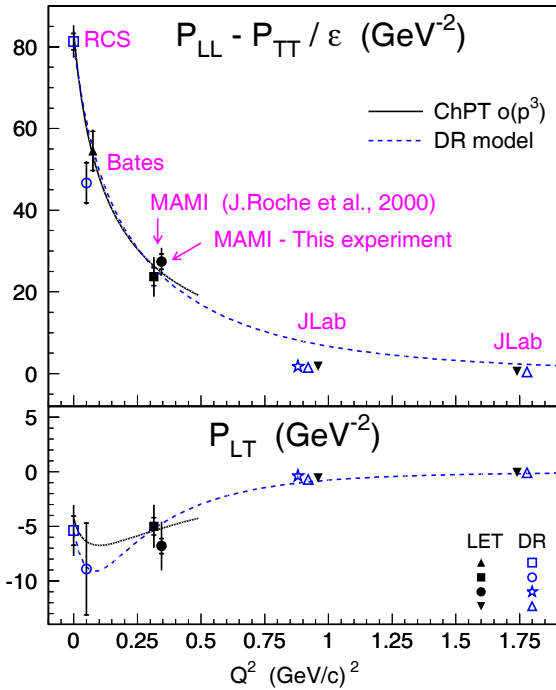


Fig. 10. The structure functions measured in this experiment (\bullet) (with the form factors of ref. [20]) and previously at Bates [10], MAMI [11], JLab [12] and in RCS [6]. The solid curve is the HBChPT calculation [24]. The dashed curve is an example of the dispersive (DR) calculation [27] with dipole ansatz parameters $(A_\alpha, A_\beta) = (1.8, 0.5)$ GeV. Curves are calculated for $\epsilon = 0.645$. Data points correspond to different ϵ (0.90 [10], 0.62 [11], 0.645 (this experiment), 0.95 and 0.88 [12]). They are obtained from either a LET analysis or a dispersive one (DR). Some points are shifted in the abscissa for visibility. The inner error bar is statistical, the outer one is the quadratic sum of statistical and systematic errors.

P_{LT} , the scalar part is proportional to $G_E^p \cdot \beta_M$. The measured points tend to confirm the existence of an extremum of β_M at low Q^2 , traditionally explained by the interplay between diamagnetic and paramagnetic contributions. To summarize, both structure functions show a non-trivial Q^2 behavior, that can be related to the pion cloud structure of the nucleon. However, experimental data are still scarce and more measurements in the Q^2 region between 0 and $1 (\text{GeV}/c)^2$ would help to gain insight into the matter.

6 Conclusion

New values for the structure functions $P_{LL} - P_{TT}/\epsilon$ and P_{LT} were obtained from the present VCS experiment performed at MAMI. Apart from a well-understood systematic difference, the results are in very good agreement with the ones obtained in the previous MAMI experiment [11]. They are also in good agreement with the calculation of HBChPT [24]. The new feature in the present analysis is an iterative procedure in the calculation of the solid angle, inducing an increase of both structure functions. The ef-

fect of different proton form factor parameterizations has also been studied in detail. More precise measurements of these form factors at low Q^2 [30,31] will help to reduce the uncertainties in the determination of the GPs. More VCS measurements at low Q^2 would help to investigate the non-trivial behavior of the GPs and their connection to the mesonic structure of the nucleon.

We would like to thank the accelerator group of MAMI for its excellent support. This work was supported in part by the FWO-Flanders (Belgium), the BOF-Gent University, the Deutsche Forschungsgemeinschaft with the Collaborative Research Center 443, the Federal State of Rhineland-Palatinate and the French CEA and CNRS/IN2P3.

References

1. H. Arenhövel, D. Drechsel, Nucl. Phys. A **233**, 153 (1974).
2. P.A.M. Guichon, G.Q. Liu, A.W. Thomas, Nucl. Phys. A **591**, 606 (1995).
3. M. Vanderhaeghen, Phys. Lett. B **402**, 243 (1997).
4. P.A.M. Guichon, M. Vanderhaeghen, Prog. Part. Nucl. Phys. **41**, 125 (1998).
5. A.I. L'vov, S. Scherer, B. Pasquini, C. Unkmeir, D. Drechsel, Phys. Rev. C **64**, 015203 (2001).
6. V. Olmos de Leon *et al.*, Eur. Phys. J. A **10**, 207 (2001).
7. N. d'Hose, H. Merkel, *Double Polarization Virtual Compton Scattering in the threshold regime at MAMI*, MAMI proposal A1-1/00 (2001).
8. P. Janssens, *Double-polarized virtual Compton scattering as a probe of the proton structure*, PhD Thesis, Universiteit Gent (2007).
9. L. Doria, *Polarization observables in virtual Compton scattering*, PhD Thesis, Universität Mainz (2008).
10. P. Bourgeois *et al.*, Phys. Rev. Lett. **97**, 212001 (2006).
11. J. Roche *et al.*, Phys. Rev. Lett. **85**, 708 (2000).
12. G. Laveissière *et al.*, Phys. Rev. Lett. **93**, 122001 (2004).
13. K.I. Blomqvist *et al.*, Nucl. Instrum. Methods A **403**, 263 (1998).
14. P. Janssens *et al.*, Nucl. Instrum. Methods A **566**, 675 (2006).
15. M. Vanderhaeghen *et al.*, Phys. Rev. C **62**, 025501 (2000).
16. J. Friedrich, T. Walcher, Eur. Phys. J. A **17**, 607 (2003).
17. P. Mergell, U. G. Meissner, D. Drechsel, Nucl. Phys. A **596**, 367 (1996).
18. H.W. Hammer, U.-G. Meissner, Eur. Phys. J. A **20**, 469 (2004).
19. M.A. Belushkin, H.W. Hammer, U.G. Meissner, Phys. Rev. C **75**, 035202 (2007).
20. G. Höhler *et al.*, Nucl. Phys. B **114**, 505 (1976).
21. J.J. Kelly, Phys. Rev. C **70**, 068202 (2004).
22. J. Arrington, W. Melnitchouk, J.A. Tjon, Phys. Rev. C **76**, 035205 (2007).
23. C.E. Hyde-Wright, K. de Jager, Annu. Rev. Nucl. Part. Sci. **54**, 217 (2004).
24. T.R. Hemmert, B.R. Holstein, G. Knochlein, D. Drechsel, Phys. Rev. D **62**, 014013 (2000).
25. C.W. Kao, M. Vanderhaeghen, Phys. Rev. Lett. **89**, 272002 (2002).
26. C.-W. Kao, B. Pasquini, M. Vanderhaeghen, Phys. Rev. D **70**, 114004 (2004).

27. B. Pasquini, M. Gorchtein, D. Drechsel, A. Metz, M. Vanderhaeghen, *Eur. Phys. J. A* **11**, 185 (2001).
28. D. Drechsel, B. Pasquini, M. Vanderhaeghen, *Phys. Rep.* **378**, 99 (2003).
29. N. d'Hose, *Eur. Phys. J. A* **28**, 117 (2006).
30. R. Gilman *et al.*, Proposal, JLab PR-07-004 (2006).
31. M.O. Distler, MAMI A1-2/05 proposal (2005).